ACS EARTH AND SPACE CHEMISTRY

http://pubs.acs.org/journal/aesccq

Article

Morphology and Viscosity Changes after Reactive Uptake of Isoprene Epoxydiols in Submicrometer Phase Separated Particles with Secondary Organic Aerosol Formed from Different Volatile Organic Compounds

Ziying Lei, Nicole E. Olson, Yue Zhang, Yuzhi Chen, Andrew T. Lambe, Jing Zhang, Natalie J. White, Joanna M. Atkin, Mark M. Banaszak Holl, Zhenfa Zhang, Avram Gold, Jason D. Surratt,* and Andrew P. Ault*

Cite This: *ACS Earth Space Chem.* 2022, 6, 871−882

Read Online

ACCESS | Metrics & More | Article Recommendations | Supporting Information

ABSTRACT: Secondary organic aerosol (SOA), formed from the oxidation of volatile organic compounds (VOCs), is a large contributor to atmospheric fine particulate matter ($PM_{2.5}$) and is commonly present in mixed inorganic−organic submicron particles. SOA formed from varying biogenic and anthropogenic VOCs results in unique aerosol physicochemical properties that modify climate impacts (i.e., water uptake). Understanding reactive uptake of VOC-derived semivolatile oxidation products to inorganic-SOA mixed particles remains limited, particularly for particles at the most abundant sizes (by number) in the atmosphere (~100 nm). These particles are challenging to study as SOA can be quite viscous (i.e., solid or semisolid), and mixed particles can have complex morphologies (e.g., core−shell). Herein, we show that the viscosity and morphology of initially core−shell (inorganic−organic) particles changed substantially after acid-catalyzed reactive uptake of isoprene epoxydiols (IEPOX), and that differences were highly dependent on VOC precursor (α-pinene, β-caryophyllene, isoprene, and toluene). SOA from two higher molecular weight precursors (α-pinene and β-caryophyllene) were less viscous after IEPOX uptake at 50% relative humidity (RH), while SOA viscosities from lower molecular weight precursors (isoprene and toluene) did not change appreciably, based on atomic force microscopy (AFM) measurements. The evolution of inorganic-SOA particle viscosity and morphology could alter the predicted impacts of SOA on air quality and climate.

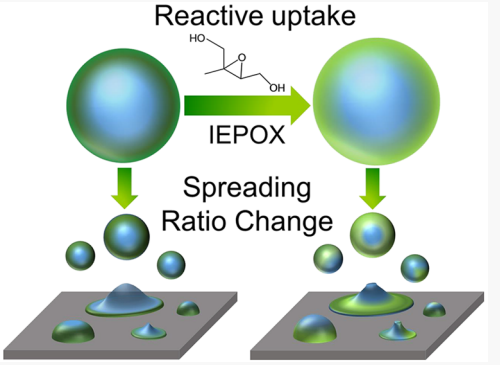

KEYWORDS: *atmospheric chemistry, secondary organic aerosol, heterogeneous chemistry, aerosol phase state, core−shell morphology, reactive uptake, atomic force microscopy, photothermal infrared spectroscopy*

INTRODUCTION

Secondary organic aerosol (SOA) constitutes a significant fraction of the global aerosol budget for fine particulate matter ($PM_{2.5}$, aerosol particles with aerodynamic diameters <2.5 μm),[1] which is the most important size range with respect to aerosol impacts on human health and climate, particularly particles ~100 nm in diameter.[2−4] SOA is primarily formed from oxidation of volatile organic compounds (VOCs), resulting in lower-vapor pressure products that either nucleate, condense, or undergo reactive uptake to existing particles (e.g., ammonium-sulfate particles).[5] Since SOA is formed from a variety of biogenic and anthropogenic VOC precursors (α-pinene, β-caryophyllene, isoprene, and toluene), this leads to SOA being composed of a wide range of chemical species with different physicochemical properties (e.g., viscosity and morphology).

Viscous SOA can increase diffusion time scales from microseconds to weeks (i.e., longer than atmospheric particle lifetimes),[6] which decreases the rate of SOA formation. For example, the reactive uptake of isoprene epoxydiols (IEPOX), a key oxidation product of isoprene,[7−9] can decrease diffusion by over an order of magnitude for viscous SOA formed on atmospherically relevant time scales (<2 days).[10−12] Koop et al. established a framework for understanding the viscosity of bulk organic material, which ranges from the dynamic viscosity (η) of liquid ($\eta < 10^2$ Pa s) to semisolid ($10^2 \leq \eta \leq 10^{12}$ Pa s)

Special Issue: Mario Molina Memorial

Received: May 23, 2021
Revised: March 1, 2022
Accepted: March 1, 2022
Published: March 23, 2022

or glassy/amorphous solid ($\eta > 10^{12}$ Pa s).[13−19] Renbaum-Wolff et al. probed viscosity as a function of relative humidity (RH) using a "bead-mobility" technique and a "poke-flow" technique for SOA derived from α-pinene,[20] isoprene,[21] and toluene,[22] which confirmed in ∼100 μm particles that SOA has a wide range of viscosities (3×10^1 to 3.7×10^8 Pa s). Organosulfates,[23−25] which are a key component of atmospheric SOA, have been shown to increase particle viscosity after incorporation of inorganic sulfate ions into organic species.[11,26] Modeling used to study SOA viscosities has continued to improve, leading to better predictions of viscosity for multicomponent mixtures and surrogate SOA mixtures derived from the oxidation of different VOC precursors.[27−29] Shiraiwa et al. have related molecular weight to glass transition temperature (T_g) and viscosity according to the number of different C, H, and O atoms and C−H and C−O bonds in a molecular formula or the molecular weight (M), oxygen-to-carbon ratio (O:C), and coefficients (A−E) (eq 1):[30]

$$T_g = A + BM + CM^2 + D(\mathrm{O{:}C}) + EM(\mathrm{O{:}C}) \quad (1)$$

Despite significant progress in understanding OA viscosity,[12,16,31−35] understanding the impacts on viscosity within individual submicron particles from different VOC precursors on reactive uptake is still limited. Recent research has shown the importance of interactions between the organic and inorganic components, such as increased propensity for semisolid aerosol due to ion−molecules interactions,[36,37] and that even in aqueous multicomponent mixtures, measured equilibration time scales can be slower than predicted by pure components using simple mixing rules.[38]

Morphology is also critical to understand SOA formation, especially as aqueous and organic components can separate into distinct phases due to the low miscibility of many SOA species within high ionic strength aqueous particles.[34,39−41] Example morphologies include homogeneous, core−shell, and partially engulfed, which all undergo reactive uptake differently, particularly when the organic phase is viscous.[11,34,42,43] For example, laboratory studies have shown a ∼50% decrease in reactive uptake of IEPOX to particles with a coating of viscous SOA from α-pinene ozonolysis ($\eta = 9.3 \times 10^7$ Pa s)[30,35] around acidic sulfate particles (pH = 1.5) versus aqueous (noncoated) acidic sulfate particles only.

Most characterization of the impacts of morphology and viscosity on reactive uptake has focused on the loss of gas-phase semivolatile organic compounds,[44] but it is also critical to understand how viscosity and morphology evolve within particles as they undergo reactive uptake. Recently, Olson et al. showed that the aqueous, sulfate-rich core of accumulation mode particles coated with α-pinene and toluene SOA was largely converted to viscous organosulfates after uptake of IEPOX in a flow tube.[26] Atmospheric chambers enable studies over longer time scales (1 min vs hours) and there have been few chamber studies probing the impact of coating viscosity and morphology on individual particles at atmospherically relevant sizes (∼100 nm).[45] Additionally, few studies have analyzed uptake to mixed organic−inorganic particles, particularly submicron particles with complex morphologies, such as core−shell types. As atmospheric chemistry models continue to improve parameterizations for accurate predictions of SOA formation rates and concentrations,[46−48] a detailed understanding of SOA formation at the single particle level is needed to provide improved modeling capabilities.

SOA from α-pinene oxidation has been the most studied coating for core−shell (inorganic−organic) particles with respect to reactive uptake,[12,15,26,49,50] but it is important to understand how SOA coatings formed from oxidation of other VOC precursors impact morphology and viscosity for a longer reaction time. Herein, we probed the viscosity and morphology of size-selected, submicron, acidic particles coated with oxidation products of four different VOC precursors (α-pinene, β-caryophyllene, isoprene, and toluene), which were subsequently injected into an atmospheric chamber and exposed to IEPOX over the course of 2 h. Individual particles were characterized using atomic force microscopy (AFM), AFM with photothermal infrared spectroscopy (AFM-PTIR), Raman microspectroscopy, and scanning electron microscopy with energy dispersive X-ray spectroscopy (SEM-EDX). Significant modification of viscosity and morphology was observed after the reactive uptake of IEPOX, which was highly dependent on the physicochemical properties of the SOA formed from the different VOC precursors examined in this study. The viscosities of α-pinene and β-caryophyllene SOA decreased significantly after IEPOX uptake, while the viscosities of isoprene and toluene SOA did not appreciably change. Phase separation occurred frequently for larger particles, and complex morphology was present for all four types of SOA particles. Overall, the changes in physicochemical properties and chemical composition of different SOA particle types after IEPOX reactive uptake increase our understanding of the impacts of multiphase chemical reactions on physicochemical properties and can lead to improved predictions of SOA formation.

METHODS

Aerosol Particle Generation and Collection. Aqueous seed particles, prior to coating with SOA, were generated from a solution of 0.06 M ammonium sulfate (Sigma-Aldrich, ≥99% purity) and 0.06 M sulfuric acid (Sigma-Aldrich, ≥98% purity) using a constant output atomizer (TSI Inc., Model 3076). This solution has a bulk pH of 1.5,[51] which was chosen based on a common pH value for submicron atmospheric particles.[52,53] Aerosol-laden air passed through one diffusion drier to remove excess water, but not to a low enough RH (i.e., RH > 40%) that they would effloresce and form solid particles. Particles with an electrical mobility diameter of 100 nm were size selected by a differential mobility analyzer (DMA, TSI Inc., Model 3080) with flow rates resulting in a semi-monodisperse size distribution.[12] They were then coated with OH-initiated oxidation products of either toluene or isoprene, or by ozonolysis products of either α-pinene or β-caryophyllene using a Potential Aerosol Mass (PAM) reactor (Aerodyne Research, Inc.).[12,26,54] Aerosol size distributions from a scanning electrical mobility spectrometer (SEMS, BMI Inc., Model 2100) were measured to ensure acidified ammonium sulfate seed particles were evenly coated with SOA and that no nucleation mode SOA particles were observed before particles were injected into the University of North Carolina at Chapel Hill (UNC) 10 m^3 indoor chamber facility.[55,56] The PAM outflow and chamber were both equilibrated to 50% RH to represent the daytime RH in the southeastern United States.[57] After SOA-coated inorganic sulfate particles were injected, the chamber was left static for at least 30 min to ensure that the aerosol particles were stable and that the chamber was uniformly mixed.[11] Then, *trans*-β-IEPOX, which was synthesized at UNC following a published procedure,[58] was dissolved

https://doi.org/10.1021/acsearthspacechem.1c00156
ACS Earth Space Chem. 2022, 6, 871−882

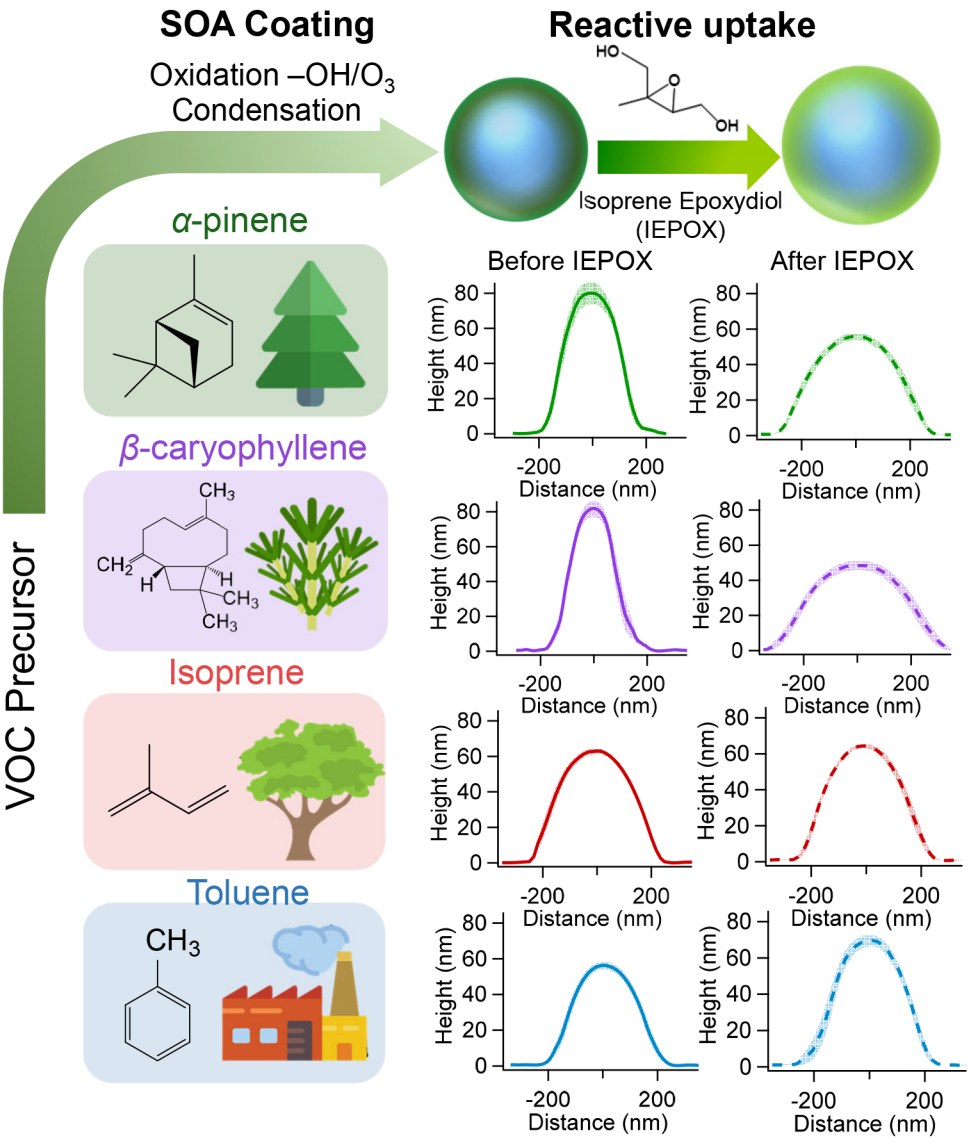

Figure 1. Experimental design showing α-pinene, β-caryophyllene, isoprene, and toluene SOA formation on acidic sulfate aerosol particles, and an average height profile of 10 particles changes before (solid lines) and after IEPOX uptake (dash lines). The shaded area for each height profile represents the uncertainty from averaging the 10 particles. Images of four VOC precursor sources are from Flaticon.com.

in ethyl acetate and gaseous IEPOX was generated by using a high-purity nitrogen flow of 2 L min^{-1} for 10 min and then 4 L min^{-1} for 50 min through a heated manifold (60 °C). This approach to introducing gaseous IEPOX into the indoor chamber has been used in previous UNC chamber studies.[11,12,26,55,59] Aerosol size distributions and number concentrations were continuously measured from the chamber to monitor particle growth using a SEMS. On the basis of the size distribution of these four types of SOA in the chamber (Figure S1), a DMA was used to select 150 nm particles formed from α-pinene, β-caryophyllene, isoprene, and toluene SOA, respectively, prior to IEPOX uptake. Additionally, 150, 200, and 250 nm SOA particles were size selected after IEPOX uptake for each VOC precursor. SOA particles were inertially impacted on silicon wafers (16013, Ted Pella Inc.) and quartz (26016, Ted Pella Inc.) substrates using a microanalysis particle sampler (MPS-3, California Measurements Inc.) at 50% RH, specifically the smallest stage with an aerodynamic diameter (d_a) < 400 nm size cut. A schematic figure showing aerosolization, coating, and UNC chamber experimental setup, along with relevant instrumentation is shown in Figure S2.

Microscopy and Spectroscopy Analysis. Individual inorganic-SOA mixed particles were analyzed to determine their size, morphology, and chemical composition using AFM, AFM-PTIR, Raman microspectroscopy, and SEM-EDX both before and after IEPOX uptake. Both AFM and Raman were conducted at room temperature (25 °C), ambient pressure, and 50% RH, while SEM images and spectra were collected under vacuum (10^{-5} to 10^{-6} Torr).

A PicoPlus 5500 AFM (Agilent, Santa Clara, CA) was used to characterize the morphology of individual inorganic-SOA mixed particles. Imaging was performed in tapping mode using Aspire CT300R probes (NanoScience; resonance frequency 300 kHz, force constant 40 N/m), to obtain height, amplitude, and phase images. The samples were scanned in 10 μm × 10 μm areas with line scans of 0.75 Hz and 512 × 512 pixels resolution. Raw data collected by AFM was processed by SPIP 6.2.6 software (Image Metrology, Hørsholm, Denmark) to

https://doi.org/10.1021/acsearthspacechem.1c00156
ACS Earth Space Chem. 2022, 6, 871−882

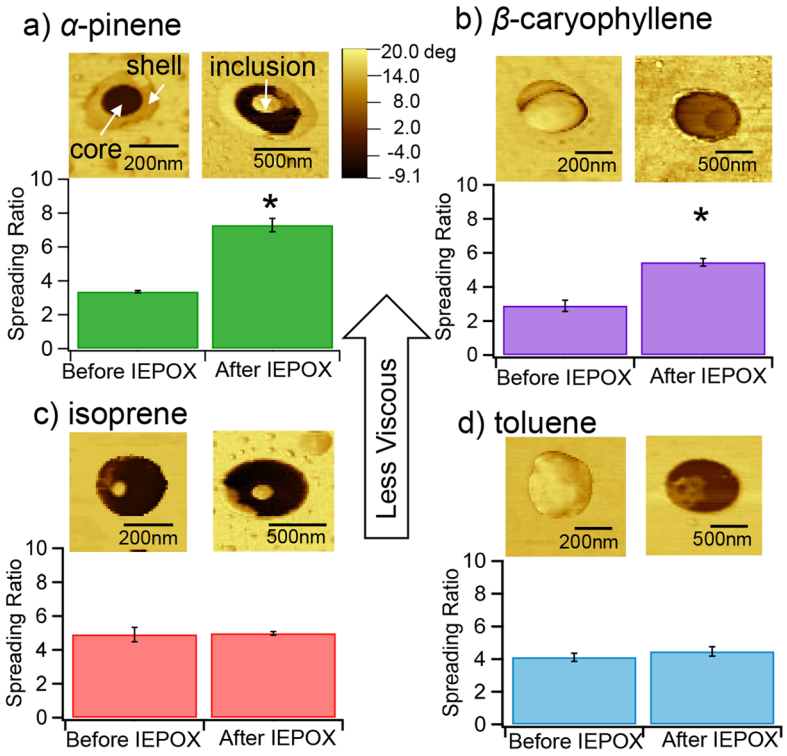

Figure 2. AFM phase images and spreading ratios of 150 nm SOA before and after IEPOX uptake. The numbers of individual particles used in the spreading ratio calculation are given in parentheses (before IEPOX and after IEPOX). (a) α-Pinene SOA (101 and 55). (b) β-Caryophyllene SOA (132 and 49 individual particles). (c) Isoprene SOA (99 and 61). (d) Toluene SOA (131 and 248). Single asterisks denote spreading ratios that are statistically different than SOA particles before IEPOX uptake ($p < 0.05$) and error bars represent $\pm \sigma$ from a Gaussian fit to the spreading ratio distribution.

measure height, projected area diameter, and volume, which is used to calculate volume equivalent diameter for individual particles. The spreading ratios of individual particles were calculated by using individual particle radius divided by particle height, as described in detail previously.[17,26] *t* tests were performed by comparing the spreading ratio of each SOA type before and after IEPOX uptake, and the spreading ratios were considered to be statistically different for *p* values <0.05.

A nanoIR2 system (Anasys Instruments, Santa Barbara, CA) was used to characterize the chemical composition of individual submicron SOA particles via photothermal infrared (PTIR) spectroscopy. AFM height, deflection images, and PTIR spectra of particles with SOA formed from toluene, α-pinene, isoprene, and β-caryophyllene after IEPOX uptake were collected in contact mode (IR power 16.54%) at a scan rate of 0.75 Hz using a gold-coated contact mode silicon nitride probe (Anasys Instruments, 13 ± 4 kHz resonant frequency, 0.07−0.4 N/m spring constant). The IR spectra were collected over a frequency range of 900−3600 cm^{-1} using a tunable IR source (2.5−12 μm, 1 kHz repetition rate, optical parametric oscillator, OPO) with a resolution of 4 cm^{-1}/point. A nanoIR3 system (Bruker, Santa Barbara, CA) with a tunable IR source (880−1950 cm^{-1} frequency range, 100 kHz repetition rate, quantum cascade laser, QCL) was used to collect PTIR spectral maps of SOA particles. Tapping-IR mode was used and the amplitude of cantilever oscillation was mapped using 128 coaverages, 400 pixels resolution. The IR ratio map was generated in Analysis Studio (Anasys Instruments software V3.15) to show differences in the spatial distribution of chemical components based on different vibrational modes.

Raman microspectroscopy was conducted using a Horiba LabRAM HR Evolution Raman Spectrometer (Horiba Scientific) equipped with a 50 mW 532 nm Nd:YAG laser source and CCD detector coupled to a confocal optical microscope (Olympus, 100× objective NA:1.25). A diffraction grating with 600 groove/mm was used to obtain a spectral resolution of 1.7 cm^{-1}. Raman spectra were collected in the range 500−4000 cm^{-1} for 3 accumulations ×15 s acquisitions for each particle.

SEM analysis was conducted on a FEI Helios 650 Nanolab Dualbeam electron microscope that operated at an accelerating voltage of 10.0 kV and a current of 0.40 nA. An Everhart−Thornley secondary electron detector was used for imaging. EDX spectra were acquired for 20 s using an EDAX Silicon Drift Detector and GENESIS EDX software version 5.10 (EDAX Inc., Mahwah, NJ), as in prior work.[26]

■ RESULTS AND DISCUSSION

Phase separated particles (organic coating around an aqueous/inorganic core) with SOA coatings from different VOC precursors (α-pinene, β-caryophyllene, isoprene, and toluene) were investigated before and after reactive uptake of IEPOX to understand the changes of individual particle morphology, phase, and viscosity (Figure 1). Models have predicted the viscosity of SOA formed from the different VOC precursors and suggest the following viscosities of α-pinene SOA (9.3×10^7 Pa s),[20,33] β-caryophyllene SOA at (3.7×10^8 Pa s),[60,61] isoprene SOA (3×10^1 to 2×10^5 Pa s),[21] and toluene SOA

https://doi.org/10.1021/acsearthspacechem.1c00156
ACS Earth Space Chem. 2022, 6, 871−882

(7.8×10^4 Pa s) at 50% RH.[22,30] Importantly, the viscosities of α-pinene and β-caryophyllene ozonolysis SOA are orders of magnitude higher than isoprene and toluene SOA from OH oxidation.[20−22,30,33,60,61] After the phase-separated SOA particles were exposed to IEPOX, particle-phase chemical reactions of IEPOX in the aqueous sulfate core formed viscous species, which can change the phase state of the core from liquid to semisolid or solid.[10,11] Different types of SOA coatings on acidic inorganic sulfate particles can change the amount of IEPOX uptake.[12] Specifically, high-viscosity SOA coatings can limit the ability of gaseous species, such as IEPOX, to diffuse into the aqueous acidic core of the particle, which will kinetically limit heterogeneous/multiphase processes and reaction rates, as well as overall particle morphology and viscosity.[10,12] The average height profile can be used as a proxy for aerosol viscosity, with taller particles representing more viscous SOA coatings.[62] The results show that α-pinene and β-caryophyllene SOA have a clear decrease in height, and thus viscosity, after IEPOX reactive uptake compared to minimal changes in height for toluene and isoprene SOA-coated particles of the same size.

Modifications to aerosol morphology and viscosity were quantitatively characterized before and after IEPOX uptake using spreading ratios calculated for size-selected 150 nm particles with α-pinene, β-caryophyllene, isoprene, and toluene SOA coatings. Changes in SOA particle viscosity were quantified by calculating the average spreading ratios of ∼100 individual particles. For α-pinene SOA, particles exhibited core−shell (inorganic−organic) morphology after coating with α-pinene ozonolysis products shown in the AFM phase images (Figure 2a), similar to previous observations.[12,63] A thicker coating was observed for 150 nm α-pinene SOA after IEPOX uptake as shown by the larger dark outer portion in the AFM phase image. The morphology of the core indicates that after IEPOX reactive uptake, the aqueous core has been converted to a semisolid or solid phase. Large spreading ratios represent liquid-like particles of lower viscosity, whereas a smaller spreading ratio suggests solid-like particles of higher viscosity.[17,26] Before IEPOX uptake, both α-pinene and β-caryophyllene SOA are more viscous than isoprene and toluene SOA with lower spreading ratios, consistent with previous studies.[20−22,61] The spreading ratio of α-pinene SOA-coated sulfate particles increased significantly after IEPOX uptake from 3.4 ± 0.1 to 7.3 ± 0.4 at 50% RH. This surprising viscosity decrease is attributed to the formation of lower molecular weight (MW) organic species from IEPOX that have lower average MWs than α-pinene SOA,[17,64−67] some of which formed in or diffused into the shell.

As indicated by AFM phase images (Figure 2b), 150 nm β-caryophyllene SOA-coated sulfate particles had partially engulfed morphology before IEPOX uptake. After IEPOX uptake, the 150 nm β-caryophyllene SOA-coated sulfate particles retained their partially engulfed morphologies, and the spreading ratio significantly increased from 2.9 ± 0.3 to 5.4 ± 0.2. β-caryophyllene has higher MW oxidation products[68−70] compared to IEPOX SOA, as with α-pinene SOA, and similarly increased spreading ratios and a lower viscosity were observed after IEPOX reactive uptake. Future work will focus on using specific species and functional groups to further characterize these changes, as opposed to MW.[71]

Isoprene SOA-coated sulfate particles (150 nm) exhibited core−shell morphologies with a thick shell both before and after IEPOX reactive uptake (Figure 2c). Spreading ratios for 150 nm isoprene SOA-coated sulfate particles are similar before and after IEPOX uptake (4.9 ± 0.4 and 4.9 ± 0.1) as the overall MW and oxidation of the SOA from IEPOX multiphase chemistry is not substantially changing the chemical composition of the shell,[72,73] resulting in similar viscosities for the same size particles.

For toluene SOA particles, a homogeneous morphology was most prevalent (Figure 2d).[26] The spreading ratios of toluene SOA-coated particles are similar before and after IEPOX uptake (4.1 ± 0.2 and 4.5 ± 0.3) at ∼50% RH, likely due to the lower MW of toluene SOA being closer to isoprene SOA than SOA from α-pinene or β-caryophyllene.[14,30,74] Larger area AFM phase images for the four types of SOA before and after IEPOX uptake with numerous particles are shown in the Supporting Information (Figure S3) to demonstrate that the individual particles shown in detail in Figure 2 are representative.

After IEPOX reactive uptake, the detailed morphology and viscosity for SOA-coated sulfate particles with different sizes were investigated. For α-pinene SOA-coated sulfate particles (Figure 3), a core−shell morphology was observed after

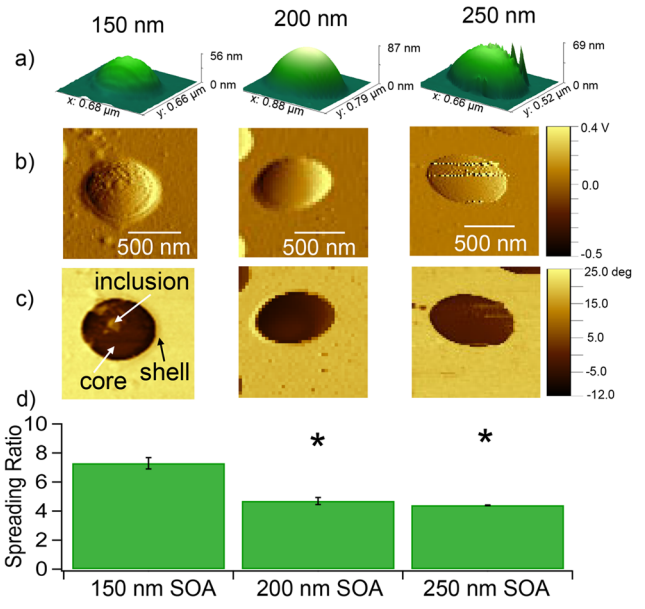

Figure 3. Morphology and the spreading ratio of size-selected α-pinene SOA before and after IEPOX uptake. (a) Representative 3D AFM images. (b) AFM amplitude images. (c) AFM phase images. (d) Bar charts show the average spreading ratio of individual particles for α-pinene SOA with 150 nm (55 particles), 200 nm (155 particles), and 250 nm (43 particles) diameters. Single asterisks denote spreading ratios of larger particles that are statistically different than 150 nm particles ($p < 0.05$) and error bars represent standard error.

IEPOX uptake (Figure 3b and 3c). Inclusions were observed for 150 nm particles, and these inclusions could be viscous organosulfates or organosulfate oligomers that salt out when sufficient amounts form.[8,11,26,55] However, the inclusions were too small for chemical analysis by the AFM-PTIR available at the time. As the particle size increased from 150 to 250 nm, the spreading ratio significantly decreased from 7.3 ± 0.4 to 4.7 ± 0.2 (Figure 3a and 3d) at ∼50% RH, indicating a more viscous particle likely due to an increase in the amount of sulfate available in the core for IEPOX to react with and form viscous species, such as organosulfates and their oligomers.[8,75−78] This

https://doi.org/10.1021/acsearthspacechem.1c00156
ACS Earth Space Chem. 2022, 6, 871−882

result is consistent with a previous study suggesting the viscosity of large (~1 μm) α-pinene SOA-coated sulfate particles increased after uptake of gaseous IEPOX.[26] β-Caryophyllene SOA-coated particles exhibited the same size-dependent spreading ratio behavior as α-pinene SOA-coated sulfate particles, with larger particles spreading less (Figure S4).

For size-selected isoprene SOA, morphology was more complex than traditional core−shell morphology, and this complex morphology was observed for both larger sizes of particles (200 and 250 nm) (Figure 4b and 4c). This suggests

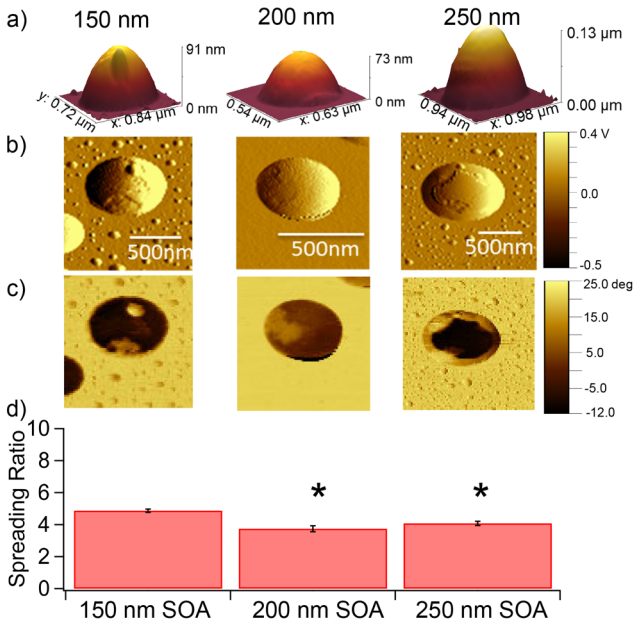

Figure 4. Morphology and the spreading ratio of size-selected isoprene SOA after IEPOX uptake. (a) Representative 3D AFM images. (b) AFM amplitude images. (c) AFM phase images. (d) Bar charts show the average spreading ratio individual particles for isoprene SOA with 150 nm (62 particles), 200 nm (87 particles), and 250 nm (128 particles) diameters. Single asterisks denote spreading ratios of larger particles that are statistically different than 150 nm particles ($p < 0.05$) and error bars represent standard error.

that the products of IEPOX reactions were distributed heterogeneously within the particles,[12,26] leading to irregular shapes. The average spreading ratio for all sizes of isoprene SOA particles ranges from 3.7 ± 0.2 to 4.9 ± 0.1 (Figure 4a and 4d) at ~50% RH. As isoprene SOA size increased from 150 to 250 nm, the spreading ratio decreased from 4.9 ± 0.1 to 4.1 ± 0.1 at ~50% RH, suggesting higher viscosity with increasing particle size. While increased viscosity was observed for α-pinene, β-caryophyllene, and isoprene SOA particles with increasing size, toluene SOA particles did not follow this trend, potentially due to toluene SOA having homogeneous morphology versus the morphologies (core−shell, partially engulfed, and complex) for the other SOA (Figure S5).

The chemical composition of individual submicron SOA particles is key to further understand the modification of SOA morphology and viscosity before and after IEPOX uptake and was analyzed using Raman microspectroscopy, AFM-PTIR, and SEM. Raman spectra were taken of the particle core and shell of α-pinene SOA-coated particles before and after IEPOX uptake (Figure 5). Before IEPOX uptake, Raman spectra showed peaks representing $\nu_s(SO_4^{2-})$ at 973, $\nu_s(HSO_4^-)$ at 1049 cm^{-1}, $\nu_s(R\text{-}OSO_3^-)$ 1074 cm^{-1}, and the broad ν(N−H) region around 3160 cm^{-1} indicating sulfate, bisulfate, α-pinene organosulfates, and ammonium located primarily in the particle core.[79−85] A carbonyl group ν(C═O) mode was observed at 1708 cm^{-1},[86] corresponding to α-pinene oxidation compounds, such as pinic acid or pinonic acid.[87−89] A peak at 1448 cm^{-1} is assigned to the methyl/methylene group bend $\delta(CH_3/CH_2)$, whereas peaks at 2882 and 2931 cm^{-1} are assigned to symmetric stretches of ν_s(C−H) of methyl groups and asymmetric stretches ν_{as}(C−H) in methylene groups, respectively.[80] The different chemical composition of the particle core and shell confirm the phase separations observed by microscopy, with acidic ammonium sulfate and some organosulfates in the particle core and organic material (α-pinene oxidation products) in the shell. An inclusion was observed for α-pinene SOA and the Raman spectrum suggests α-pinene organosulfates can be produced during the formation of the shell, which could explain the inclusions were observed in AFM images (Figure 3b and 3c). After IEPOX uptake, IEPOX-derived organosulfate formation is observed by $\nu_s(R\text{-}OSO_3^-)$ at 1060 cm^{-1}, which has been characterized previously,[26,77] and peaks between 2800 to 3000 cm^{-1} indicative of the C−H stretching region. The shape of the C−H stretching region also shifts, from modes at 2931 and 2972 before IEPOX to modes at 2880 and 2842 being most prominent afterward, indicative of changes to the organic material in the shell (more symmetric methyl and methylene stretches). Raman spectra for toluene, isoprene, and β-caryophyllene SOA-coated sulfate particles before and after IEPOX show similar results as for α-pinene SOA, and are discussed in the Supporting Information (Figure S6, S7, S8). For β-caryophyllene SOA-coated sulfate particles after IEPOX uptake, a mode was observed at 975 cm^{-1}, which could indicate some inorganic sulfate and associated water in the organic portion of the particle, which could also increase spreading. EDX spectra were consistent with Raman spectra after IEPOX reactive uptake and showed sulfate and oxygen present in the particle cores (indicative of inorganic sulfate and/or organosulfate species), with carbon and oxygen primarily present in the shell (Figure S9).

IR spectra were collected for 250 nm toluene and β-caryophyllene SOA-coated sulfate particles after IEPOX uptake using AFM-PTIR (Figure 6a). A strong peak at 1104 cm^{-1} was observed, which corresponds to the highly IR-active anti-symmetric stretch of inorganic sulfate ions, $\nu_{as}(SO_4^{2-})$, in the particle core.[90] The peaks at 1420 cm^{-1} for a β-caryophyllene SOA-coated particle and 1436 cm^{-1} for a toluene SOA-coated particle are assigned to ammonium $\delta(NH_4^+)$.[90] A less intense N−H stretch of ammonium at 3136 cm^{-1} was also observed.[90] The peaks detected at 1072 and 1068 cm^{-1} suggest the formation of organosulfates, $\nu_s(R\text{-}OSO_3^-)$.[77] A symmetric methyl stretch $\nu_s(CH_3)$ was observed at 2880 cm^{-1} for the β-caryophyllene SOA-coated particle, and an organic peak at 3060 cm^{-1} is assigned to unsaturated C−H moieties (i.e., less sp^3 hybridized) within the organic species of the C−H stretching region.[80] Peaks >3150 cm^{-1} correspond to O−H stretching.[86,91] As shown in Figure 6b, IR spectra of 250 nm isoprene SOA particle core and shell after IEPOX uptake display two strong modes, 1100 and 1424 cm^{-1} suggestive of $\nu_{as}(SO_4^{2-})$ and $\delta(NH_4^+)$, respectively,[90] in the particle core. A weak mode, ν(C═O) at 1690 cm^{-1} was observed in both core and shell. The complex core of isoprene SOA (Figure 6c)

https://doi.org/10.1021/acsearthspacechem.1c00156
ACS Earth Space Chem. 2022, 6, 871−882

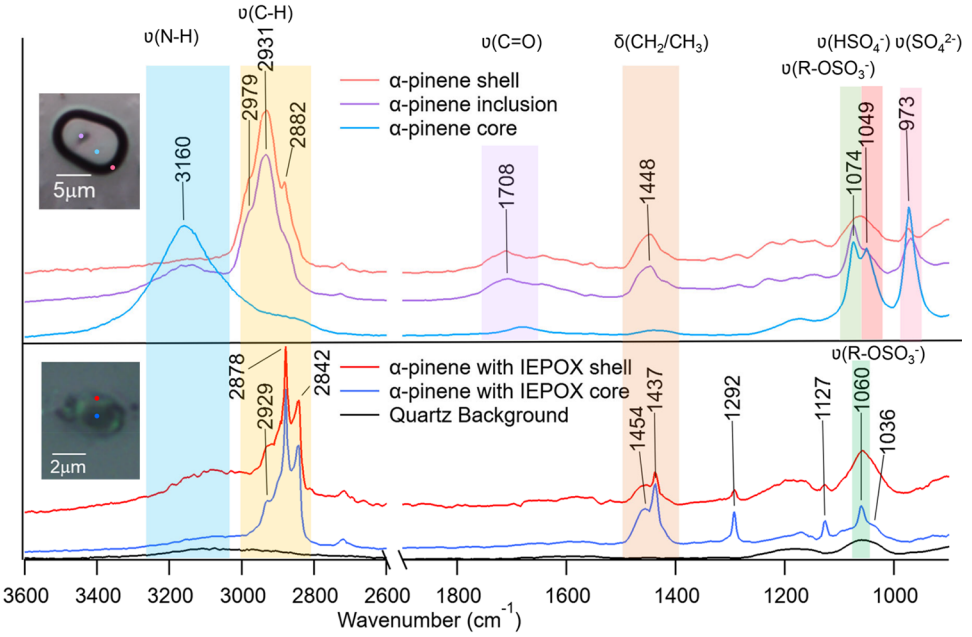

Figure 5. Raman spectra of representative α-pinene SOA core and shell before IEPOX uptake (top). Representative α-pinene SOA core and shell after IEPOX uptake (bottom). The color dots in the optical images represent the different locations of Raman spectra that were collected.

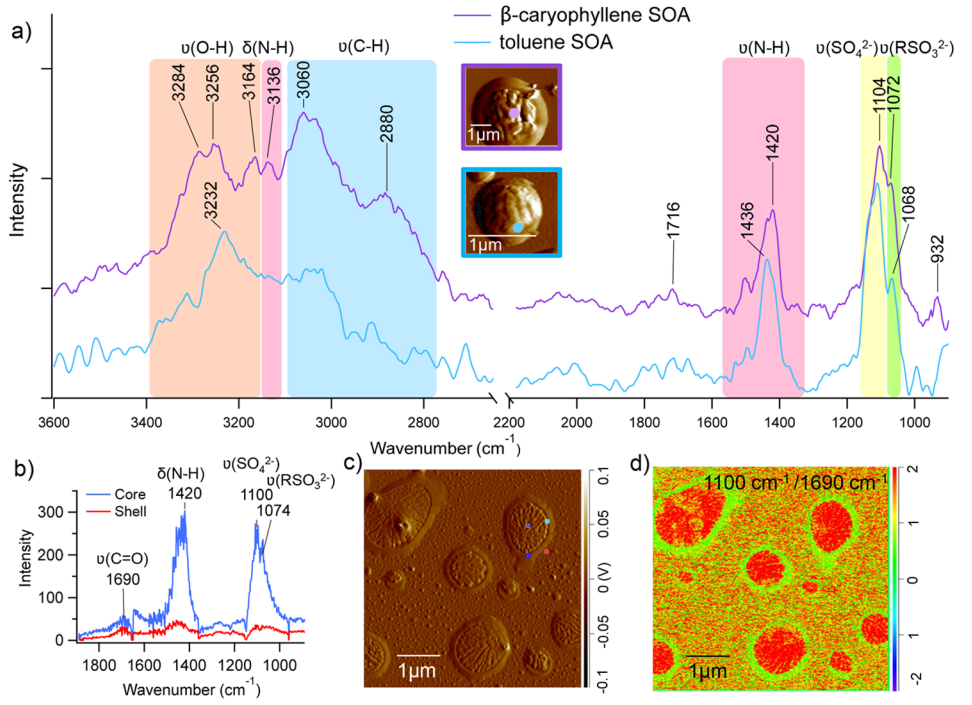

Figure 6. (a) AFM-PTIR spectra of β-caryophyllene SOA-coated and toluene SOA-coated particles after IEPOX uptake with AFM amplitude images. (b) IR spectra of isoprene SOA core and shell after IEPOX uptake. (c) AFM amplitude image of isoprene SOA after IEPOX uptake. (d) IR ratio map of 1100 cm^{-1}/1690 cm^{-1} for isoprene SOA after IEPOX uptake.

suggests that some IEPOX diffused into the particle and reacted with inorganic sulfate. To directly visualize relative differences in the spatial distribution of sulfate and organic species between the core and shell of isoprene SOA-coated sulfate particles, a ratio map (Figure 6d) was generated using 1100 cm^{-1}/1690 cm^{-1}. The areas enriched in sulfate (1100 cm^{-1}) appear red (this may include some organosulfates due to the peak widths and the proximity of the 1100 and 1074 cm^{-1} peak), while those with enhanced carbonyl concentrations (1690 cm^{-1}) appear green. The ratio map confirms that most sulfate is in the particle core and isoprene-derived organic materials are in the shell, which is consistent with Raman and EDX spectra.

Atmospheric Implications. To understand the atmospheric impact of IEPOX uptake onto SOA-coated acidic sulfate particles, SOA coatings from different VOC precursors need to be understood. The viscosity and morphology of size-selected SOA formed from four different VOC precursors (α-pinene, β-

https://doi.org/10.1021/acsearthspacechem.1c00156
ACS Earth Space Chem. 2022, 6, 871−882

caryophyllene, isoprene, and toluene) before and after IEPOX uptake have been investigated in this study. The results demonstrate that changes in viscosity and morphology of initial inorganic core-SOA shell particles after IEPOX reactive uptake are strongly dependent on VOC precursor. α-Pinene and β-caryophyllene SOA-coated sulfate particles became less viscous after IEPOX uptake, while the viscosity of isoprene and toluene SOA-coated sulfate particles did not change appreciably after IEPOX uptake. This is attributed to lower molecular weight products forming that are less viscous, as predicted by eq 1, though greater inorganic sulfate or organosulfates in the shell could increase water and contribute to the decrease in viscosity. The changes in particle viscosity can affect IEPOX diffusion and mixing time scales, which may alter SOA lifetime and the production of further SOA in these mixed organic–inorganic particles (i.e., self-limiting further atmospheric aging[11,17]). Additionally, different SOA particle sizes after IEPOX uptake (150, 200, and 250 nm from initially 150 nm particles) have been investigated, with phase separation and more particles with complex morphology being observed at larger particle sizes.[26,92] After IEPOX uptake, the larger particles were more viscous for α-pinene, β-caryophyllene, and isoprene SOA-coated sulfate particles, indicating particle size could play an important role in morphology, affecting subsequent heterogeneous reactions. Evidence accumulates that semisolid phases and individual particle properties can limit diffusion and heterogeneous reactions in organic–inorganic particles.[36−38,93] In addition, unexpected properties of submicron aerosol, such as high acidity[52,53] and increased pressure,[94] continue to paint an increasingly complicated picture of organic–inorganic particle behavior. This makes VOC- and size-dependent morphology and viscosity changes even more important to consider given their important role in overall aerosol mixing state,[95−98] as well as cloud condensation nuclei (CCN)[99] and ice nucleating particle (INP) activity,[19,100,101] which are important in cloud formation.[102−104]

■ ASSOCIATED CONTENT

Supporting Information

The Supporting Information is available free of charge at https://pubs.acs.org/doi/10.1021/acsearthspacechem.1c00156.

Additional information on the size distribution of four types of SOA particles before and after IEPOX uptake (Figure S1); schematic graph of experimental design and instrumental setup (Figure S2); AFM phase images of four types of SOA particles before and after IEPOX uptake (Figure S3); morphology and the spreading ratio of size-selected β-caryophyllene SOA particles after IEPOX uptake (Figure S4); morphology and the spreading ratio of size-selected toluene SOA particles after IEPOX uptake (Figure S5); Raman spectra of individual SOA particles after exposed to gaseous IEPOX including β-caryophyllene SOA (Figure S6), isoprene SOA (Figure S7), and toluene SOA (Figure S8); SEM images and EDX spectra of four types of SOA after IEPOX (Figure S9) (PDF)

■ AUTHOR INFORMATION

Corresponding Authors

Andrew P. Ault − *Department of Chemistry, University of Michigan, Ann Arbor, Michigan 48109, United States;* orcid.org/0000-0002-7313-8559; Email: aulta@umich.edu

Jason D. Surratt − *Department of Environmental Sciences and Engineering, University of North Carolina at Chapel Hill, Chapel Hill, North Carolina 27599, United States; Department of Chemistry, University of North Carolina at Chapel Hill, Chapel Hill, North Carolina 27599, United States;* orcid.org/0000-0002-6833-1450; Email: surratt@unc.edu

Authors

Ziying Lei − *Department of Environmental Health Sciences, University of Michigan, Ann Arbor, Michigan 48109, United States;* orcid.org/0000-0003-3071-0698

Nicole E. Olson − *Department of Chemistry, University of Michigan, Ann Arbor, Michigan 48109, United States;* orcid.org/0000-0003-1600-8050

Yue Zhang − *Department of Environmental Sciences and Engineering, University of North Carolina at Chapel Hill, Chapel Hill, North Carolina 27599, United States; Aerodyne Research Inc., Billerica, Massachusetts 01821, United States*

Yuzhi Chen − *Department of Environmental Sciences and Engineering, University of North Carolina at Chapel Hill, Chapel Hill, North Carolina 27599, United States*

Andrew T. Lambe − *Aerodyne Research Inc., Billerica, Massachusetts 01821, United States;* orcid.org/0000-0003-3031-701X

Jing Zhang − *Department of Chemical Engineering, Monash University, Melbourne, Victoria 3800, Australia*

Natalie J. White − *Department of Chemistry, University of Michigan, Ann Arbor, Michigan 48109, United States*

Joanna M. Atkin − *Department of Chemistry, University of North Carolina at Chapel Hill, Chapel Hill, North Carolina 27599, United States;* orcid.org/0000-0002-1211-5193

Mark M. Banaszak Holl − *Department of Chemical Engineering, Monash University, Melbourne, Victoria 3800, Australia;* orcid.org/0000-0001-7759-7456

Zhenfa Zhang − *Department of Environmental Sciences and Engineering, University of North Carolina at Chapel Hill, Chapel Hill, North Carolina 27599, United States*

Avram Gold − *Department of Environmental Sciences and Engineering, University of North Carolina at Chapel Hill, Chapel Hill, North Carolina 27599, United States*

Complete contact information is available at: https://pubs.acs.org/10.1021/acsearthspacechem.1c00156

Funding

This work was supported by the National Science Foundation (NSF) through Grants AGS-1703019 (Ault) and AGS-1703535 (Surratt). A.G., Z.Z., and J.D.S. also acknowledge support from NSF Grant No. AGS-2001027 (Gold). Y.Z. acknowledges support from the NSF-AGS Postdoctoral Fellowship (Grant No. 1524731).

Notes

The authors declare no competing financial interest.

■ ACKNOWLEDGMENTS

The authors would like to thank the Michigan Center for Materials Characterization (MC^2) for access to and assistance with the SEM-EDX, which is supported by the University of Michigan College of Engineering. The authors acknowledge

the Scanning Probe Microscopy facility in Department of Chemistry at the University of Michigan.

REFERENCES

(1) Shiraiwa, M.; Li, Y.; Tsimpidi, A. P.; Karydis, V. A.; Berkemeier, T.; Pandis, S. N.; Lelieveld, J.; Koop, T.; Pöschl, U. Global distribution of particle phase state in atmospheric secondary organic aerosols. *Nat. Commun.* **2017**, *8* (1), 15002.

(2) Shiraiwa, M.; Ueda, K.; Pozzer, A.; Lammel, G.; Kampf, C. J.; Fushimi, A.; Enami, S.; Arangio, A. M.; Fröhlich-Nowoisky, J.; Fujitani, Y.; Furuyama, A.; Lakey, P. S. J.; Lelieveld, J.; Lucas, K.; Morino, Y.; Pöschl, U.; Takahama, S.; Takami, A.; Tong, H.; Weber, B.; Yoshino, A.; Sato, K. Aerosol Health Effects from Molecular to Global Scales. *Environ. Sci. Technol.* **2017**, *51* (23), 13545−13567.

(3) Pope, C. A.; Dockery, D. W. Health Effects of Fine Particulate Air Pollution: Lines that Connect. *J. Air Waste Manage. Assoc.* **2006**, *56* (6), 709−742.

(4) Ren-Jian, Z.; Kin-Fai, H.; Zhen-Xing, S. The Role of Aerosol in Climate Change, the Environment, and Human Health. *Atmos. Oceanic Sci. Lett.* **2012**, *5* (2), 156−161.

(5) Carlton, A. M.; Wiedinmyer, C.; Kroll, J. A review of Secondary Organic Aerosol (SOA) formation from isoprene. *Atmos. Chem. Phys* **2009**, *9*, 4987.

(6) Virtanen, A.; Joutsensaari, J.; Koop, T.; Kannosto, J.; Yli-Pirilä, P.; Leskinen, J.; Mäkelä, J. M.; Holopainen, J. K.; Pöschl, U.; Kulmala, M.; Worsnop, D. R.; Laaksonen, A. An amorphous solid state of biogenic secondary organic aerosol particles. *Nature* **2010**, *467* (7317), 824−827.

(7) Surratt, J. D.; Chan, A. W. H.; Eddingsaas, N. C.; Chan, M.; Loza, C. L.; Kwan, A. J.; Hersey, S. P.; Flagan, R. C.; Wennberg, P. O.; Seinfeld, J. H. Reactive intermediates revealed in secondary organic aerosol formation from isoprene. *Proc. Natl. Acad. Sci. U. S. A.* **2010**, *107* (15), 6640.

(8) Surratt, J. D.; Gómez-González, Y.; Chan, A. W. H.; Vermeylen, R.; Shahgholi, M.; Kleindienst, T. E.; Edney, E. O.; Offenberg, J. H.; Lewandowski, M.; Jaoui, M.; Maenhaut, W.; Claeys, M.; Flagan, R. C.; Seinfeld, J. H. Organosulfate Formation in Biogenic Secondary Organic Aerosol. *J. Phys. Chem. A* **2008**, *112* (36), 8345−8378.

(9) Surratt, J. D.; Murphy, S. M.; Kroll, J. H.; Ng, N. L.; Hildebrandt, L.; Sorooshian, A.; Szmigielski, R.; Vermeylen, R.; Maenhaut, W.; Claeys, M.; Flagan, R. C.; Seinfeld, J. H. Chemical Composition of Secondary Organic Aerosol Formed from the Photooxidation of Isoprene. *J. Phys. Chem. A* **2006**, *110* (31), 9665−9690.

(10) Zhang, Y.; Chen, Y.; Lei, Z.; Olson, N. E.; Riva, M.; Koss, A. R.; Zhang, Z.; Gold, A.; Jayne, J. T.; Worsnop, D. R.; Onasch, T. B.; Kroll, J. H.; Turpin, B. J.; Ault, A. P.; Surratt, J. D. Joint Impacts of Acidity and Viscosity on the Formation of Secondary Organic Aerosol from Isoprene Epoxydiols (IEPOX) in Phase Separated Particles. *ACS Earth Space Chem.* **2019**, *3* (12), 2646−2658.

(11) Riva, M.; Chen, Y.; Zhang, Y.; Lei, Z.; Olson, N. E.; Boyer, H. C.; Narayan, S.; Yee, L. D.; Green, H. S.; Cui, T.; Zhang, Z.; Baumann, K.; Fort, M.; Edgerton, E.; Budisulistiorini, S. H.; Rose, C. A.; Ribeiro, I. O.; e Oliveira, R. L.; dos Santos, E. O.; Machado, C. M. D.; Szopa, S.; Zhao, Y.; Alves, E. G.; de Sá, S. S.; Hu, W.; Knipping, E. M.; Shaw, S. L.; Duvoisin Junior, S.; de Souza, R. A. F.; Palm, B. B.; Jimenez, J.-L.; Glasius, M.; Goldstein, A. H.; Pye, H. O. T.; Gold, A.; Turpin, B. J.; Vizuete, W.; Martin, S. T.; Thornton, J. A.; Dutcher, C. S.; Ault, A. P.; Surratt, J. D. Increasing Isoprene Epoxydiol-to-Inorganic Sulfate Aerosol Ratio Results in Extensive Conversion of Inorganic Sulfate to Organosulfur Forms: Implications for Aerosol Physicochemical Properties. *Environ. Sci. Technol.* **2019**, *53* (15), 8682−8694.

(12) Zhang, Y.; Chen, Y.; Lambe, A. T.; Olson, N. E.; Lei, Z.; Craig, R. L.; Zhang, Z.; Gold, A.; Onasch, T. B.; Jayne, J. T.; Worsnop, D. R.; Gaston, C. J.; Thornton, J. A.; Vizuete, W.; Ault, A. P.; Surratt, J. D. Effect of the Aerosol-Phase State on Secondary Organic Aerosol Formation from the Reactive Uptake of Isoprene-Derived Epoxydiols (IEPOX). *Env. Sci. Tech. Lett.* **2018**, *5* (3), 167−174.

(13) Zobrist, B.; Marcolli, C.; Pedernera, D. A.; Koop, T. Do atmospheric aerosols form glasses? *Atmos. Chem. Phys.* **2008**, *8* (17), 5221−5244.

(14) Koop, T.; Bookhold, J.; Shiraiwa, M.; Pöschl, U. Glass transition and phase state of organic compounds: dependency on molecular properties and implications for secondary organic aerosols in the atmosphere. *Phys. Chem. Chem. Phys.* **2011**, *13* (43), 19238−19255.

(15) Huang, W.; Saathoff, H.; Pajunoja, A.; Shen, X.; Naumann, K. H.; Wagner, R.; Virtanen, A.; Leisner, T.; Mohr, C. α-Pinene secondary organic aerosol at low temperature: chemical composition and implications for particle viscosity. *Atmos. Chem. Phys.* **2018**, *18* (4), 2883−2898.

(16) Reid, J.; Bertram, A.; Topping, D.; Laskin, A.; Martin, S.; Petters, M.; Pope, F.; Rovelli, G. The viscosity of atmospherically relevant organic particles. *Nat. Commun.* **2018**, DOI: 10.1038/s41467-018-03027-z.

(17) Slade, J. H.; Ault, A. P.; Bui, A. T.; Ditto, J. C.; Lei, Z.; Bondy, A. L.; Olson, N. E.; Cook, R. D.; Desrochers, S. J.; Harvey, R. M.; Erickson, M. H.; Wallace, H. W.; Alvarez, S. L.; Flynn, J. H.; Boor, B. E.; Petrucci, G. A.; Gentner, D. R.; Griffin, R. J.; Shepson, P. B. Bouncier Particles at Night: Biogenic Secondary Organic Aerosol Chemistry and Sulfate Drive Diel Variations in the Aerosol Phase in a Mixed Forest. *Environ. Sci. Technol.* **2019**, *53* (9), 4977−4987.

(18) Zhang, Y.; Katira, S.; Lee, A.; Lambe, A. T.; Onasch, T. B.; Xu, W.; Brooks, W. A.; Canagaratna, M. R.; Freedman, A.; Jayne, J. T.; Worsnop, D. R.; Davidovits, P.; Chandler, D.; Kolb, C. E. Kinetically controlled glass transition measurement of organic aerosol thin films using broadband dielectric spectroscopy. *Atmos. Meas. Technol.* **2018**, *11* (6), 3479−3490.

(19) Zhang, Y.; Nichman, L.; Spencer, P.; Jung, J. I.; Lee, A.; Heffernan, B. K.; Gold, A.; Zhang, Z.; Chen, Y.; Canagaratna, M. R.; Jayne, J. T.; Worsnop, D. R.; Onasch, T. B.; Surratt, J. D.; Chandler, D.; Davidovits, P.; Kolb, C. E. The Cooling Rate- and Volatility-Dependent Glass-Forming Properties of Organic Aerosols Measured by Broadband Dielectric Spectroscopy. *Environ. Sci. Technol.* **2019**, *53* (21), 12366−12378.

(20) Renbaum-Wolff, L.; Grayson, J. W.; Bateman, A. P.; Kuwata, M.; Sellier, M.; Murray, B. J.; Shilling, J. E.; Martin, S. T.; Bertram, A. K. Viscosity of a-pinene secondary organic material and implications for particle growth and reactivity. *Proc. Natl. Acad. Sci. U. S. A.* **2013**, *110* (20), 8014.

(21) Song, M.; Liu, P.; Hanna, S.; Li, Y.; Martin, S.; Bertram, A. Relative humidity-dependent viscosities of isoprene-derived secondary organic material and atmospheric implications for isoprene-dominant forests. *Atmos. Chem. Phys.* **2015**, *15*, 5145.

(22) Song, M.; Liu, P. F.; Hanna, S. J.; Zaveri, R. A.; Potter, K.; You, Y.; Martin, S. T.; Bertram, A. K. Relative humidity-dependent viscosity of secondary organic material from toluene photo-oxidation and possible implications for organic particulate matter over megacities. *Atmos. Chem. Phys.* **2016**, *16* (14), 8817−8830.

(23) Hatch, L. E.; Creamean, J. M.; Ault, A. P.; Surratt, J. D.; Chan, M. N.; Seinfeld, J. H.; Edgerton, E. S.; Su, Y. X.; Prather, K. A. Measurements of Isoprene-Derived Organosulfates in Ambient Aerosols by Aerosol Time-of-Flight Mass Spectrometry-Part 2: Temporal Variability and Formation Mechanisms. *Environ. Sci. Technol.* **2011**, *45* (20), 8648−8655.

(24) Surratt, J. D.; Kroll, J. H.; Kleindienst, T. E.; Edney, E. O.; Claeys, M.; Sorooshian, A.; Ng, N. L.; Offenberg, J. H.; Lewandowski, M.; Jaoui, M.; Flagan, R. C.; Seinfeld, J. H. Evidence for organosulfates in secondary organic aerosol. *Environ. Sci. Technol.* **2007**, *41* (2), 517−527.

(25) Hettiyadura, A. P. S.; Al-Naiema, I. M.; Hughes, D. D.; Fang, T.; Stone, E. A. Organosulfates in Atlanta, Georgia: anthropogenic influences on biogenic secondary organic aerosol formation. *Atmos. Chem. Phys.* **2019**, *19* (5), 3191−3206.

(26) Olson, N. E.; Lei, Z.; Craig, R. L.; Zhang, Y.; Chen, Y.; Lambe, A. T.; Zhang, Z.; Gold, A.; Surratt, J. D.; Ault, A. P. Reactive Uptake of Isoprene Epoxydiols Increases the Viscosity of the Core of Phase-

Separated Aerosol Particles. *ACS Earth Space Chem.* **2019**, *3* (8), 1402−1414.
(27) Li, Y.; Day, D. A.; Stark, H.; Jimenez, J. L.; Shiraiwa, M. Predictions of the glass transition temperature and viscosity of organic aerosols from volatility distributions. *Atmos. Chem. Phys.* **2020**, *20* (13), 8103−8122.
(28) Tikkanen, O. P.; Hämäläinen, V.; Rovelli, G.; Lipponen, A.; Shiraiwa, M.; Reid, J. P.; Lehtinen, K. E. J.; Yli-Juuti, T. Optimization of process models for determining volatility distribution and viscosity of organic aerosols from isothermal particle evaporation data. *Atmos. Chem. Phys.* **2019**, *19* (14), 9333−9350.
(29) Gervasi, N. R.; Topping, D. O.; Zuend, A. A predictive group-contribution model for the viscosity of aqueous organic aerosol. *Atmos. Chem. Phys.* **2020**, *20* (5), 2987−3008.
(30) DeRieux, W. S. W.; Li, Y.; Lin, P.; Laskin, J.; Laskin, A.; Bertram, A. K.; Nizkorodov, S. A.; Shiraiwa, M. Predicting the glass transition temperature and viscosity of secondary organic material using molecular composition. *Atmos. Chem. Phys.* **2018**, *18* (9), 6331−6351.
(31) Schmedding, R.; Rasool, Q. Z.; Zhang, Y.; Pye, H. O. T.; Zhang, H.; Chen, Y.; Surratt, J. D.; Lopez-Hilfiker, F. D.; Thornton, J. A.; Goldstein, A. H.; Vizuete, W. Predicting secondary organic aerosol phase state and viscosity and its effect on multiphase chemistry in a regional-scale air quality model. *Atmos. Chem. Phys.* **2020**, *20* (13), 8201−8225.
(32) Marcolli, C.; Krieger, U. K. Relevance of Particle Morphology for Atmospheric Aerosol Processing. *Trends Chem.* **2020**, *2* (1), 1−3.
(33) Järvinen, E.; Ignatius, K.; Nichman, L.; Kristensen, T.; Fuchs, C.; Höppel, N.; Corbin, J.; Craven, J.; Duplissy, J.; Ehrhart, S.; Haddad, I.; Frege, C.; Gates, S.; Gordon, H.; Hoyle, C.; Jokinen, T.; Kallinger, P.; Kirkby, J.; Kiselev, A.; Schnaiter, M. Observation of viscosity transition in α-pinene secondary organic aerosol. *Atmos. Chem. Phys. Discuss.* **2015**, *15*, 28575−28617.
(34) Freedman, M. A. Phase separation in organic aerosol. *Chem. Soc. Rev.* **2017**, *46* (24), 7694−7705.
(35) Zhang, Y.; Sanchez, M. S.; Douet, C.; Wang, Y.; Bateman, A. P.; Gong, Z.; Kuwata, M.; Renbaum-Wolff, L.; Sato, B. B.; Liu, P. F.; Bertram, A. K.; Geiger, F. M.; Martin, S. T. Changing shapes and implied viscosities of suspended submicron particles. *Atmos. Chem. Phys.* **2015**, *15* (14), 7819−7829.
(36) Richards, D. S.; Trobaugh, K. L.; Hajek-Herrera, J.; Price, C. L.; Sheldon, C. S.; Davies, J. F.; Davis, R. D. Ion−molecule interactions enable unexpected phase transitions in organic-inorganic aerosol. *Sci. Adv.* **2020**, *6* (47), No. eabb5643.
(37) Lee, C.; Dommer, A. C.; Schiffer, J. M.; Amaro, R. E.; Grassian, V. H.; Prather, K. A. Cation-Driven Lipopolysaccharide Morphological Changes Impact Heterogeneous Reactions of Nitric Acid with Sea Spray Aerosol Particles. *J. Phys. Chem. Lett.* **2021**, *12* (20), 5023−5029.
(38) Wallace, B. J.; Price, C. L.; Davies, J. F.; Preston, T. C. Multicomponent diffusion in atmospheric aerosol particles. *Environ. Sci.: Atmos.* **2021**, *1* (1), 45−55.
(39) You, Y.; Renbaum-Wolff, L.; Carreras-Sospedra, M.; Hanna, S. J.; Hiranuma, N.; Kamal, S.; Smith, M. L.; Zhang, X.; Weber, R. J.; Shilling, J. E.; Dabdub, D.; Martin, S. T.; Bertram, A. K. Images reveal that atmospheric particles can undergo liquid-liquid phase separations. *Proc. Natl. Acad. Sci. U. S. A.* **2012**, *109* (33), 13188.
(40) Freedman, M. A. Liquid-Liquid Phase Separation in Supermicrometer and Submicrometer Aerosol Particles. *Acc. Chem. Res.* **2020**, *53* (6), 1102−1110.
(41) O'Brien, R. E.; Wang, B.; Kelly, S. T.; Lundt, N.; You, Y.; Bertram, A. K.; Leone, S. R.; Laskin, A.; Gilles, M. K. Liquid-Liquid Phase Separation in Aerosol Particles: Imaging at the Nanometer Scale. *Environ. Sci. Technol.* **2015**, *49* (8), 4995−5002.
(42) Song, M.; Marcolli, C.; Krieger, U. K.; Lienhard, D. M.; Peter, T. Morphologies of mixed organic/inorganic/aqueous aerosol droplets. *Faraday Discuss.* **2013**, *165* (0), 289−316.
(43) Kwamena, N. O. A.; Buajarern, J.; Reid, J. P. Equilibrium Morphology of Mixed Organic/Inorganic/Aqueous Aerosol Droplets: Investigating the Effect of Relative Humidity and Surfactants. *J. Phys. Chem. A* **2010**, *114* (18), 5787−5795.
(44) Shiraiwa, M.; Zuend, A.; Bertram, A. K.; Seinfeld, J. H. Gas-particle partitioning of atmospheric aerosols: interplay of physical state, non-ideal mixing and morphology. *Phys. Chem. Chem. Phys.* **2013**, *15* (27), 11441−11453.
(45) O'Brien, R. E.; Neu, A.; Epstein, S. A.; MacMillan, A. C.; Wang, B.; Kelly, S. T.; Nizkorodov, S. A.; Laskin, A.; Moffet, R. C.; Gilles, M. K. Physical properties of ambient and laboratory-generated secondary organic aerosol. *Geophys. Res. Lett.* **2014**, *41* (12), 4347−4353.
(46) Hallquist, M.; Wenger, J. C.; Baltensperger, U.; Rudich, Y.; Simpson, D.; Claeys, M.; Dommen, J.; Donahue, N. M.; George, C.; Goldstein, A. H.; Hamilton, J. F.; Herrmann, H.; Hoffmann, T.; Iinuma, Y.; Jang, M.; Jenkin, M. E.; Jimenez, J. L.; Kiendler-Scharr, A.; Maenhaut, W.; McFiggans, G.; Mentel, T. F.; Monod, A.; Prévôt, A. S. H.; Seinfeld, J. H.; Surratt, J. D.; Szmigielski, R.; Wildt, J. The formation, properties and impact of secondary organic aerosol: current and emerging issues. *Atmos. Chem. Phys.* **2009**, *9* (14), 5155−5236.
(47) Carlton, A. G.; Wiedinmyer, C.; Kroll, J. H. A review of Secondary Organic Aerosol (SOA) formation from isoprene. *Atmos. Chem. Phys.* **2009**, *9* (14), 4987−5005.
(48) Tsigaridis, K.; Daskalakis, N.; Kanakidou, M.; Adams, P. J.; Artaxo, P.; Bahadur, R.; Balkanski, Y.; Bauer, S. E.; Bellouin, N.; Benedetti, A.; Bergman, T.; Berntsen, T. K.; Beukes, J. P.; Bian, H.; Carslaw, K. S.; Chin, M.; Curci, G.; Diehl, T.; Easter, R. C.; Ghan, S. J.; Gong, S. L.; Hodzic, A.; Hoyle, C. R.; Iversen, T.; Jathar, S.; Jimenez, J. L.; Kaiser, J. W.; Kirkevåg, A.; Koch, D.; Kokkola, H.; Lee, Y. H.; Lin, G.; Liu, X.; Luo, G.; Ma, X.; Mann, G. W.; Mihalopoulos, N.; Morcrette, J. J.; Müller, J. F.; Myhre, G.; Myriokefalitakis, S.; Ng, N. L.; O'Donnell, D.; Penner, J. E.; Pozzoli, L.; Pringle, K. J.; Russell, L. M.; Schulz, M.; Sciare, J.; Seland, Ø.; Shindell, D. T.; Sillman, S.; Skeie, R. B.; Spracklen, D.; Stavrakou, T.; Steenrod, S. D.; Takemura, T.; Tiitta, P.; Tilmes, S.; Tost, H.; van Noije, T.; van Zyl, P. G.; von Salzen, K.; Yu, F.; Wang, Z.; Wang, Z.; Zaveri, R. A.; Zhang, H.; Zhang, K.; Zhang, Q.; Zhang, X. The AeroCom evaluation and intercomparison of organic aerosol in global models. *Atmos. Chem. Phys.* **2014**, *14* (19), 10845−10895.
(49) Song, M.; Ham, S.; Andrews, R. J.; You, Y.; Bertram, A. K. Liquid-liquid phase separation in organic particles containing one and two organic species: importance of the average O: C. *Atmos. Chem. Phys.* **2018**, *18* (16), 12075−12084.
(50) Song, M.; Marcolli, C.; Krieger, U. K.; Zuend, A.; Peter, T. Liquid-liquid phase separation and morphology of internally mixed dicarboxylic acids/ammonium sulfate/water particles. *Atmos. Chem. Phys.* **2012**, *12* (5), 2691−2712.
(51) Craig, R. L.; Peterson, P. K.; Nandy, L.; Lei, Z.; Hossain, M. A.; Camarena, S.; Dodson, R. A.; Cook, R. D.; Dutcher, C. S.; Ault, A. P. Direct Determination of Aerosol pH: Size-Resolved Measurements of Submicrometer and Supermicrometer Aqueous Particles. *Anal. Chem.* **2018**, *90* (19), 11232−11239.
(52) Pye, H. O. T.; Nenes, A.; Alexander, B.; Ault, A. P.; Barth, M. C.; Clegg, S. L.; Collett, J. L., Jr; Fahey, K. M.; Hennigan, C. J.; Herrmann, H.; Kanakidou, M.; Kelly, J. T.; Ku, I. T.; McNeill, V. F.; Riemer, N.; Schaefer, T.; Shi, G.; Tilgner, A.; Walker, J. T.; Wang, T.; Weber, R.; Xing, J.; Zaveri, R. A.; Zuend, A. The acidity of atmospheric particles and clouds. *Atmos. Chem. Phys.* **2020**, *20* (8), 4809−4888.
(53) Zheng, G.; Su, H.; Wang, S.; Andreae, M. O.; Pöschl, U.; Cheng, Y. Multiphase buffer theory explains contrasts in atmospheric aerosol acidity. *Science* **2020**, *369* (6509), 1374−1377.
(54) Lambe, A. T.; Ahern, A. T.; Williams, L. R.; Slowik, J. G.; Wong, J. P. S.; Abbatt, J. P. D.; Brune, W. H.; Ng, N. L.; Wright, J. P.; Croasdale, D. R.; Worsnop, D. R.; Davidovits, P.; Onasch, T. B. Characterization of aerosol photooxidation flow reactors: heterogeneous oxidation, secondary organic aerosol formation and cloud condensation nuclei activity measurements. *Atmos. Meas. Technol.* **2011**, *4* (3), 445−461.

https://doi.org/10.1021/acsearthspacechem.1c00156
ACS Earth Space Chem. 2022, 6, 871−882

(55) Lin, Y.-H.; Zhang, Z.; Docherty, K. S.; Zhang, H.; Budisulistiorini, S. H.; Rubitschun, C. L.; Shaw, S. L.; Knipping, E. M.; Edgerton, E. S.; Kleindienst, T. E.; Gold, A.; Surratt, J. D. Isoprene Epoxydiols as Precursors to Secondary Organic Aerosol Formation: Acid-Catalyzed Reactive Uptake Studies with Authentic Compounds. *Environ. Sci. Technol.* **2012**, *46* (1), 250−258.
(56) Riva, M.; Budisulistiorini, S. H.; Zhang, Z.; Gold, A.; Surratt, J. D. Chemical characterization of secondary organic aerosol constituents from isoprene ozonolysis in the presence of acidic aerosol. *Atmos. Environ.* **2016**, *130*, 5−13.
(57) Guo, H.; Xu, L.; Bougiatioti, A.; Cerully, K. M.; Capps, S. L.; Hite, J. R.; Carlton, A. G.; Lee, S. H.; Bergin, M. H.; Ng, N. L.; Nenes, A.; Weber, R. J. Fine-particle water and pH in the southeastern United States. *Atmos. Chem. Phys.* **2015**, *15* (9), 5211−5228.
(58) Zhang, Z.; Lin, Y. H.; Zhang, H.; Surratt, J. D.; Ball, L. M.; Gold, A. Technical Note: Synthesis of isoprene atmospheric oxidation products: isomeric epoxydiols and the rearrangement products *cis*- and *trans*-3-methyl-3,4-dihydroxytetrahydrofuran. *Atmos. Chem. Phys.* **2012**, *12* (18), 8529−8535.
(59) Riedel, T. P.; Lin, Y.-H.; Budisulistiorini, S. H.; Gaston, C. J.; Thornton, J. A.; Zhang, Z.; Vizuete, W.; Gold, A.; Surratt, J. D. Heterogeneous Reactions of Isoprene-Derived Epoxides: Reaction Probabilities and Molar Secondary Organic Aerosol Yield Estimates. *Environ. Sci. Technol. Lett.* **2015**, *2* (2), 38−42.
(60) Champion, W. M.; Rothfuss, N. E.; Petters, M. D.; Grieshop, A. P. Volatility and Viscosity Are Correlated in Terpene Secondary Organic Aerosol Formed in a Flow Reactor. *Environ. Sci. Technol. Lett.* **2019**, *6* (9), 513−519.
(61) Maclean, A. M.; Smith, N. R.; Li, Y.; Huang, Y.; Hettiyadura, A. P. S.; Crescenzo, G. V.; Shiraiwa, M.; Laskin, A.; Nizkorodov, S. A.; Bertram, A. K. Humidity-Dependent Viscosity of Secondary Organic Aerosol from Ozonolysis of β-Caryophyllene: Measurements, Predictions, and Implications. *ACS Earth Space Chem.* **2021**, *5* (2), 305−318.
(62) Ray, K. K.; Lee, H. D.; Gutierrez, M. A.; Chang, F. J.; Tivanski, A. V. Correlating 3D Morphology, Phase State, and Viscoelastic Properties of Individual Substrate-Deposited Particles. *Anal. Chem.* **2019**, *91* (12), 7621−7630.
(63) Robinson, E. S.; Saleh, R.; Donahue, N. M. Probing the Evaporation Dynamics of Mixed SOA/Squalane Particles Using Size-Resolved Composition and Single-Particle Measurements. *Environ. Sci. Technol.* **2015**, *49* (16), 9724−9732.
(64) Gao, S.; Keywood, M.; Ng, N. L.; Surratt, J.; Varutbangkul, V.; Bahreini, R.; Flagan, R. C.; Seinfeld, J. H. Low-Molecular-Weight and Oligomeric Components in Secondary Organic Aerosol from the Ozonolysis of Cycloalkenes and α-Pinene. *J. Phys. Chem. A* **2004**, *108* (46), 10147−10164.
(65) Docherty, K. S.; Wu, W.; Lim, Y. B.; Ziemann, P. J. Contributions of Organic Peroxides to Secondary Aerosol Formed from Reactions of Monoterpenes with O3. *Environ. Sci. Technol.* **2005**, *39* (11), 4049−4059.
(66) Tolocka, M. P.; Jang, M.; Ginter, J. M.; Cox, F. J.; Kamens, R. M.; Johnston, M. V. Formation of Oligomers in Secondary Organic Aerosol. *Environ. Sci. Technol.* **2004**, *38* (5), 1428−1434.
(67) Witkowski, B.; Gierczak, T. Early stage composition of SOA produced by α-pinene/ozone reaction: α-Acyloxyhydroperoxy aldehydes and acidic dimers. *Atmos. Environ.* **2014**, *95*, 59−70.
(68) Kundu, S.; Fisseha, R.; Putman, A. L.; Rahn, T. A.; Mazzoleni, L. R. Molecular formula composition of β-caryophyllene ozonolysis SOA formed in humid and dry conditions. *Atmos. Environ.* **2017**, *154*, 70−81.
(69) Kanawati, B.; Herrmann, F.; Joniec, S.; Winterhalter, R.; Moortgat, G. Mass spectrometric characterization of β -caryophyllene ozonolysis products in the aerosol studied using an electrospray triple quadrupole and time-of-flight analyzer hybrid system and density functional theory. *Rapid Commun. Mass Spectrom.* **2008**, *22*, 165−86.
(70) Kahnt, A.; Vermeylen, R.; Iinuma, Y.; Safi Shalamzari, M.; Maenhaut, W.; Claeys, M. High-molecular-weight esters in α-pinene ozonolysis secondary organic aerosol: structural characterization and mechanistic proposal for their formation from highly oxygenated molecules. *Atmos. Chem. Phys.* **2018**, *18* (11), 8453−8467.
(71) D'Ambro, E. L.; Lee, B. H.; Liu, J.; Shilling, J. E.; Gaston, C. J.; Lopez-Hilfiker, F. D.; Schobesberger, S.; Zaveri, R. A.; Mohr, C.; Lutz, A.; Zhang, Z.; Gold, A.; Surratt, J. D.; Rivera-Rios, J. C.; Keutsch, F. N.; Thornton, J. A. Molecular composition and volatility of isoprene photochemical oxidation secondary organic aerosol under low- and high-NOx conditions. *Atmos. Chem. Phys.* **2017**, *17* (1), 159−174.
(72) Gaston, C. J.; Riedel, T. P.; Zhang, Z.; Gold, A.; Surratt, J. D.; Thornton, J. A. Reactive Uptake of an Isoprene-Derived Epoxydiol to Submicron Aerosol Particles. *Environ. Sci. Technol.* **2014**, *48* (19), 11178−11186.
(73) Surratt, J. D.; Chan, A. W. H.; Eddingsaas, N. C.; Chan, M.; Loza, C. L.; Kwan, A. J.; Hersey, S. P.; Flagan, R. C.; Wennberg, P. O.; Seinfeld, J. H. Reactive intermediates revealed in secondary organic aerosol formation from isoprene. *Proc. Natl. Acad. Sci. U. S. A.* **2010**, *107* (15), 6640−6645.
(74) Song, M.; Liu, P. F.; Hanna, S. J.; Martin, S. T.; Bertram, A. K. Relative humidity-dependent viscosities of isoprene-derived secondary organic material and atmospheric implications for isoprene-dominant forests. *Atmos. Chem. Phys. Discuss.* **2015**, *15* (1), 1131−1169.
(75) Budisulistiorini, S. H.; Nenes, A.; Carlton, A. G.; Surratt, J. D.; McNeill, V. F.; Pye, H. O. T. Simulating Aqueous-Phase Isoprene-Epoxydiol (IEPOX) Secondary Organic Aerosol Production During the 2013 Southern Oxidant and Aerosol Study (SOAS). *Environ. Sci. Technol.* **2017**, *51* (9), 5026−5034.
(76) Surratt, J. D.; Chan, A. W.; Eddingsaas, N. C.; Chan, M.; Loza, C. L.; Kwan, A. J.; Hersey, S. P.; Flagan, R. C.; Wennberg, P. O.; Seinfeld, J. H. Reactive intermediates revealed in secondary organic aerosol formation from isoprene. *Proc. Natl. Acad. Sci. U. S. A.* **2010**, *107* (15), 6640−5.
(77) Bondy, A. L.; Craig, R. L.; Zhang, Z.; Gold, A.; Surratt, J. D.; Ault, A. P. Isoprene-Derived Organosulfates: Vibrational Mode Analysis by Raman Spectroscopy, Acidity-Dependent Spectral Modes, and Observation in Individual Atmospheric Particles. *J. Phys. Chem. A* **2018**, *122* (1), 303−315.
(78) Riva, M.; Bell, D. M.; Hansen, A.-M. K.; Drozd, G. T.; Zhang, Z.; Gold, A.; Imre, D.; Surratt, J. D.; Glasius, M.; Zelenyuk, A. Effect of Organic Coatings, Humidity and Aerosol Acidity on Multiphase Chemistry of Isoprene Epoxydiols. *Environ. Sci. Technol.* **2016**, *50* (11), 5580−5588.
(79) Craig, R. L.; Bondy, A. L.; Ault, A. P. Computer-controlled Raman microspectroscopy (CC-Raman): A method for the rapid characterization of individual atmospheric aerosol particles. *Aerosol Sci. Technol.* **2017**, *51* (9), 1099−1112.
(80) Ault, A. P.; Zhao, D.; Ebben, C. J.; Tauber, M. J.; Geiger, F. M.; Prather, K. A.; Grassian, V. H. Raman microspectroscopy and vibrational sum frequency generation spectroscopy as probes of the bulk and surface compositions of size-resolved sea spray aerosol particles. *Phys. Chem. Chem. Phys.* **2013**, *15* (17), 6206−14.
(81) Venkateswarlu, P.; Bist, H. D.; Jain, Y. S. Laser excited Raman spectrum of ammonium sulfate single crystal. *J. Raman Spectrosc.* **1975**, *3* (2−3), 143−151.
(82) Vargas Jentzsch, P.; Kampe, B.; Ciobota, V.; Rosch, P.; Popp, J. Inorganic salts in atmospheric particulate matter: Raman spectroscopy as an analytical tool. *Spectrochim Acta A Mol. Biomol Spectrosc* **2013**, *115*, 697−708.
(83) Sobanska, S.; Hwang, H.; Choël, M.; Jung, H.-J.; Eom, H.-J.; Kim, H.; Barbillat, J.; Ro, C.-U. Investigation of the Chemical Mixing State of Individual Asian Dust Particles by the Combined Use of Electron Probe X-ray Microanalysis and Raman Microspectrometry. *Anal. Chem.* **2012**, *84* (7), 3145−3154.
(84) Zhou, Q.; Pang, S.-F.; Wang, Y.; Ma, J.-B.; Zhang, Y.-H. Confocal Raman Studies of the Evolution of the Physical State of Mixed Phthalic Acid/Ammonium Sulfate Aerosol Droplets and the Effect of Substrates. *J. Phys. Chem. B* **2014**, *118* (23), 6198−6205.
(85) Hyttinen, N.; Elm, J.; Malila, J.; Calderón, S. M.; Prisle, N. L. Thermodynamic properties of isoprene- and monoterpene-derived

organosulfates estimated with COSMOtherm. *Atmos. Chem. Phys.* **2020**, *20* (9), 5679−5696.
(86) Larkin, P. *Infrared and Raman Spectroscopy: Principles and Spectral Interpretation*; Elsevier: Amsterdam, Boston, 2011; p 228.
(87) Feltracco, M.; Barbaro, E.; Contini, D.; Zangrando, R.; Toscano, G.; Battistel, D.; Barbante, C.; Gambaro, A. Photo-oxidation products of α-pinene in coarse, fine and ultrafine aerosol: A new high sensitive HPLC-MS/MS method. *Atmos. Environ.* **2018**, *180*, 149−155.
(88) Yu, J.; Cocker, D. R.; Griffin, R. J.; Flagan, R. C.; Seinfeld, J. H. Gas-Phase Ozone Oxidation of Monoterpenes: Gaseous and Particulate Products. *Journal of Atmospheric Chemistry* **1999**, *34* (2), 207−258.
(89) Cahill, T. M.; Seaman, V. Y.; Charles, M. J.; Holzinger, R.; Goldstein, A. H. Secondary organic aerosols formed from oxidation of biogenic volatile organic compounds in the Sierra Nevada Mountains of California. *J. Geophys. Res.* **2006**, DOI: 10.1029/2006JD007178.
(90) Bondy, A. L.; Kirpes, R. M.; Merzel, R. L.; Pratt, K. A.; Banaszak Holl, M. M.; Ault, A. P. Atomic Force Microscopy-Infrared Spectroscopy of Individual Atmospheric Aerosol Particles: Subdiffraction Limit Vibrational Spectroscopy and Morphological Analysis. *Anal. Chem.* **2017**, *89* (17), 8594−8598.
(91) Ault, A. P.; Guasco, T. L.; Baltrusaitis, J.; Ryder, O. S.; Trueblood, J. V.; Collins, D. B.; Ruppel, M. J.; Cuadra-Rodriguez, L. A.; Prather, K. A.; Grassian, V. H. Heterogeneous reactivity of nitric acid with nascent sea spray aerosol: large differences observed between and within individual particles. *J. Phys. Chem. Lett.* **2014**, *5*, 2493−2500.
(92) Veghte, D. P.; Altaf, M. B.; Freedman, M. A. Size dependence of the structure of organic aerosol. *J. Am. Chem. Soc.* **2013**, *135* (43), 16046−9.
(93) Ushijima, S. B.; Huynh, E.; Davis, R. D.; Tolbert, M. A. Seeded Crystal Growth of Internally Mixed Organic-Inorganic Aerosols: Impact of Organic Phase State. *J. Phys. Chem. A* **2021**, *125* (39), 8668−8679.
(94) Riva, M.; Sun, J.; McNeill, V. F.; Ragon, C.; Perrier, S.; Rudich, Y.; Nizkorodov, S. A.; Chen, J.; Caupin, F.; Hoffmann, T.; George, C. High Pressure Inside Nanometer-Sized Particles Influences the Rate and Products of Chemical Reactions. *Environ. Sci. Technol.* **2021**, *55* (12), 7786−7793.
(95) Riemer, N.; Ault, A. P.; West, M.; Craig, R. L.; Curtis, J. H. Aerosol Mixing State: Measurements, Modeling, and Impacts. *Rev. Geophys.* **2019**, *57* (2), 187−249.
(96) Bauer, S. E.; Ault, A.; Prather, K. A. Evaluation of aerosol mixing state classes in the GISS modelE-MATRIX climate model using single-particle mass spectrometry measurements. *J. Geophys. Res.: Atmos.* **2013**, *118* (17), 9834−9844.
(97) Bondy, A. L.; Bonanno, D.; Moffet, R. C.; Wang, B.; Laskin, A.; Ault, A. P. The diverse chemical mixing state of aerosol particles in the southeastern United States. *Atmos. Chem. Phys.* **2018**, *18* (16), 12595−12612.
(98) Kirpes, R. M.; Bondy, A. L.; Bonanno, D.; Moffet, R. C.; Wang, B.; Laskin, A.; Ault, A. P.; Pratt, K. A. Secondary sulfate is internally mixed with sea spray aerosol and organic aerosol in the winter Arctic. *Atmos. Chem. Phys.* **2018**, *18* (6), 3937−3949.
(99) Pierce, J. R.; Leaitch, W. R.; Liggio, J.; Westervelt, D. M.; Wainwright, C. D.; Abbatt, J. P. D.; Ahlm, L.; Al-Basheer, W.; Cziczo, D. J.; Hayden, K. L.; Lee, A. K. Y.; Li, S. M.; Russell, L. M.; Sjostedt, S. J.; Strawbridge, K. B.; Travis, M.; Vlasenko, A.; Wentzell, J. J. B.; Wiebe, H. A.; Wong, J. P. S.; Macdonald, A. M. Nucleation and condensational growth to CCN sizes during a sustained pristine biogenic SOA event in a forested mountain valley. *Atmos. Chem. Phys.* **2012**, *12* (7), 3147−3163.
(100) Wolf, M. J.; Zhang, Y.; Zawadowicz, M. A.; Goodell, M.; Froyd, K.; Freney, E.; Sellegri, K.; Rösch, M.; Cui, T.; Winter, M.; Lacher, L.; Axisa, D.; DeMott, P. J.; Levin, E. J. T.; Gute, E.; Abbatt, J.; Koss, A.; Kroll, J. H.; Surratt, J. D.; Cziczo, D. J. A biogenic secondary organic aerosol source of cirrus ice nucleating particles. *Nat. Commun.* **2020**, *11* (1), 4834.
(101) Murray, B. J.; Wilson, T. W.; Dobbie, S.; Cui, Z.; Al-Jumur, S. M. R. K.; Möhler, O.; Schnaiter, M.; Wagner, R.; Benz, S.; Niemand, M.; Saathoff, H.; Ebert, V.; Wagner, S.; Kärcher, B. Heterogeneous nucleation of ice particles on glassy aerosols under cirrus conditions. *Nat. Geosci.* **2010**, *3* (4), 233−237.
(102) Ehn, M.; Thornton, J. A.; Kleist, E.; Sipilä, M.; Junninen, H.; Pullinen, I.; Springer, M.; Rubach, F.; Tillmann, R.; Lee, B.; Lopez-Hilfiker, F.; Andres, S.; Acir, I.-H.; Rissanen, M.; Jokinen, T.; Schobesberger, S.; Kangasluoma, J.; Kontkanen, J.; Nieminen, T.; Kurtén, T.; Nielsen, L. B.; Jørgensen, S.; Kjaergaard, H. G.; Canagaratna, M.; Maso, M. D.; Berndt, T.; Petäjä, T.; Wahner, A.; Kerminen, V.-M.; Kulmala, M.; Worsnop, D. R.; Wildt, J.; Mentel, T. F. A large source of low-volatility secondary organic aerosol. *Nature* **2014**, *506* (7489), 476−479.
(103) Scott, C. E.; Spracklen, D. V.; Pierce, J. R.; Riipinen, I.; D'Andrea, S. D.; Rap, A.; Carslaw, K. S.; Forster, P. M.; Artaxo, P.; Kulmala, M.; Rizzo, L. V.; Swietlicki, E.; Mann, G. W.; Pringle, K. J. Impact of gas-to-particle partitioning approaches on the simulated radiative effects of biogenic secondary organic aerosol. *Atmos. Chem. Phys.* **2015**, *15* (22), 12989−13001.
(104) Riipinen, I.; Yli-Juuti, T.; Pierce, J. R.; Petäjä, T.; Worsnop, D. R.; Kulmala, M.; Donahue, N. M. The contribution of organics to atmospheric nanoparticle growth. *Nat. Geosci.* **2012**, *5* (7), 453−458.